IEEE Access
Multidisciplinary ⋮ Rapid Review ⋮ Open Access Journal

Received 16 May 2024, accepted 22 June 2024, date of publication 26 June 2024, date of current version 5 July 2024.

Digital Object Identifier 10.1109/ACCESS.2024.3419234

RESEARCH ARTICLE

An Online Single-Ended Traveling Waves Fault Detection Algorithm for High-Voltage Multi-Branch Overhead Lines

SEBASTIAN DAMBONE SESSA[1], (Member, IEEE), FRANCESCO SANNITI[1], (Member, IEEE), ALESSANDRO GRECO[2], SIMONE TALOMO[2], MARTINA PAJUSSIN[2], AND ROBERTO BENATO[1], (Senior Member, IEEE)

[1]Department of Industrial Engineering, University of Padova, 35131 Padua, Italy
[2]Terna, 00156 Rome, Italy

Corresponding author: Sebastian Dambone Sessa (sebastian.dambonesessa@unipd.it)

This work was supported by Terna S.p.A. by means of the "Consorzio Interuniversitario Nazionale Energia e Sistemi Elettrici" (ENSIEL) under Grant DSC007.

ABSTRACT This paper proposes a novel single-ended traveling wave-based fault location method for unearthed overhead lines with a complex topology. The low fault current magnitudes of a phase-to-ground fault in unearthed sub-transmission networks make ineffective the operation of the impedance-based protection. The proposed method decouples the dependence of the traveling waves propagation modes on the speed propagation of the line, to release the analysis of a multi-branched non-homogeneous line by means of a single measurement terminal. The combination of the results obtained by analyzing different propagation modes allows to determine the fault distance with errors in the order of tens of meters. The proposed method has been applied to a multi-terminal and branched unearthed overhead line simulated in EMTP-RV environment to identify 20 different faults, 10 before the line branch and 10 after it. In the majority of the tested fault cases, the proposed technique allows identifying the fault location with an average error lower than 0.3%. For faults in critical positions, for instance close to the line branch or to the measurement terminal, the average error is lower than 10%.

INDEX TERMS Traveling wave, continuous wavelet transform, speed propagation, unearthed overhead lines.

I. INTRODUCTION

A. MOTIVATIONS

This work focuses on a new single-ended Traveling Wave Based (TWB) fault location method for Over Head Lines (OHLs) with a complex topology. The studies which focus on the development of effective and accurate methods to identify the fault position in high voltage (HV) OHLs are having a growing interest in the power systems research field. This is because, the correct and quick identification of the fault position is essential to increase the availability of OHLs and of the electrical network, in turn. In fact, a high level of transmission line availability is a key point to guarantee the network stability especially in the frame of the energy transition from fossil fuel to renewable energy sources [1]. Moreover, reliable fault location procedures significantly reduce the costs to identify the position of a permanent fault. This is particularly true when the causes or the effects of a fault are difficult to identify by means of a visual inspection. This is the typical situation of phase-to-ground faults in unearthed (or compensated) OHL sub-transmission networks, which are characterized by very low fault current magnitudes and which are mainly caused by the cracking of porcelain insulators, which is extremely difficult to see [2].

In this context, the challenge is to develop reliable algorithms to derive the fault position information from the analysis of the fault current or voltages registered by suitable measurement devices, characterized by a suitable sample rate.

The associate editor coordinating the review of this manuscript and approving it for publication was Wei Xu.

From the other hand, it is also important to limit the costs necessary to equip power transmission lines with such fault location tools.

B. LITERATURE REVIEW

The technical literature offers several techniques to locate the position of faults in OHLs or hybrid transmission lines, which are based on different physical principles. In summary, the most common classification of such methods divides them into Impedance Based (IB), Artificial Intelligence Based (AIB) and TWB.

IB methods are effective and relatively simple to implement in earthed networks [3], [4], [5], but they are quite challenging to apply in unearthed ones, since the fault current is usually small compared to the load one [3], [6]. One of the main difficulties in this approach lies in the fault distance estimation without knowing the fault impedance. Interesting researches in this field are carried out in [7], [8], and [9]. Moreover, in [10], [11], and [12] the problem of identifying the fault distance in unearthed network is discussed.

AIB methods are especially suitable for networks with a complex topology. The most common approach is to start from current or voltage measurements which are then processed by a neural network or a learning algorithm. In general, several measurement devices are necessary to acquire the data that must be processed by the AI algorithms to identify the fault position, and so they are typically applied to distribution networks.

Through the approach presented in [13], several machine learning algorithms are applied to detect the fault position in a transmission network through the application of voltage phasors registered during the fault by means of virtual PMUs simulated in Real-Time Digital Simulator.

In [14] micro-phasor measurement units are exploited to locate the fault position in distribution networks by means of a novel machine learning method. This method only uses the recorded voltage at the sub-station and distributed generators. In [15] the back propagation neural network approach is optimized by combining the genetic algorithm and cloud theory to identify the fault position in distribution networks. In [16], the fault position is estimated by training an adaptive neuro-fuzzy inference system which receives as input the current measured at the substation. The main limitation of this procedures is the necessity of training the algorithms each time the monitoring system is installed, by limiting the flexibility of the methodology for different networks.

Regarding the TWB fault location methods, the technical literature presents promising approaches which are applied to OHLs or hybrid transmission lines. TWB methods are based on the analyzes of the propagations and reflections of the current or voltage traveling waves which are generated whenever a fault occurs. Most methods start from the decomposition of the fault voltages or currents in their propagation modes, i.e. the aerials and the earth propagation ones, and then process the signals by exploiting different techniques.

A first typology of TWB methods is represented by the double-ended approaches, which require at least two measurement terminals, one at each end of the monitored line [17]. From one hand, the presence of two or more measurement terminals makes a complex network topology easy to analyze, from the other hand this solution is more expensive compared to the single-ended techniques.

In the double-ended method proposed in [18] the successive variational mode decomposition is applied to the aerial mode of the fault voltages, in order to obtain their intrinsic mode functions. The method also requires the identification of the TW propagation speed, which is obtained by the frequency–velocity characteristic curve. By considering the time-domain and frequency-dependent characteristics of traveling wave, the fault distance is estimated by combining the arrival time, frequency and propagation velocity.

In [19], a non-contact measurement of traveling wave is proposed, in order to achieve accurate fault location and time of arrival detection on a two-terminal overhead transmission line. Such method exploits the magnetic field sensor array on each tower to measure the quality of current traveling waves generated on the transmission line and locate the transient disturbances after the occurrence of a short circuit. The results show that in a the PSCAD/MATLAB simulation environment the proposed method is very accurate.

In [20] the Maximum Mean Discrepancy approach is used to categorize different transmission lines, and then a double-ended convolutional neural network and long short-term memory combination model is built for similar lines. The fault features are extracted in an end-to-end form, and the weights of combination model are determined by the Q-learning algorithm to finally identify the fault position.

In [21] the effect of the sampling frequency on two-terminal TWB methods is analyzed. The paper demonstrates how such effect can be represented by well-defined regions in a time-space diagram and that there is an error component associated with the sampling frequency which has to be considered in double-ended TWB fault location approaches in order to improve them.

In [22], authors present a fault location algorithm which does not require the two-end data to be synchronized and which does not require to compute the TW propagation velocity. To identify the fault position, the time difference between the arrival of the first incident fault-induced TW and the successive reflection from the fault point is computed at each line end, separately.

Differently from the double-ended techniques, single-ended approaches are able to detect the fault by starting from one measurement terminal. The main research challenge for these methods is to deal with complex line topologies, considering multi-terminal or branched lines with frequent changes in the OHL tower configuration along the line route and the presence of line in electromagnetic parallel with the monitored OHL. In fact, such complex topologies determine significant changes in the line surge impedance,

by determining several TW reflections, and consequently introducing different speed propagation.

Hence, it is difficult to correctly correlate the TWs detected by the single measurement device with the points along the line where they have been transmitted or reflected. For this reason, several contributions in literature apply the single-ended fault location approach to only two terminal lines, with no branches and without considering the change of the tower configurations along the line route. In this context, an interesting approach is presented in [23], which is able to consider hybrid transmission lines where the fault distance is obtained by exploiting the detected arrival times of the voltage TWs and their polarities.

This approach exploits the Wavelet transform to analyze the fault transient voltage and it is not affected by the chosen mother wavelet type. In [2], the authors develop a method which exploits the earth-mode current to identify the fault position for unearthed overhead lines with a simple topology.

In [24] a location function describing the energy distribution of traveling-wave catastrophe is exploited to derive the fault position. The method is proven to be robust for non-branched lines, but it requires improvement to be effective in presence of branched lines.

The approach proposed in [25] processes the outputs taken from different single-ended phasor-based fault location techniques. To properly select the algorithms to be used in the proposed solution, a Real-Time Digital Simulator is used to carry out massive hardware-in-the-loop fault simulations on test power systems. The main advantage of this method lies on the fact that beyond estimating the fault distance, it provides reliable fault search fields, which are useful to improve the accuracy in locating the fault position. For simple transmission line configurations, the method demonstrated to be effective.

In [26], a novel function to estimate the time delay between the fault-induced incident and reflected signals is exploited to estimate the fault distance. The proposed method does not depend on pre-classification of the fault type and it is not affected by the low frequencies that may show up in the correlation function output. Besides, it only needs the first incident surge to be detected at the monitored bus. There are also few contributions which analyze single-ended methods applied to branched or multi-terminal lines. In [27], the ratio of alpha-mode to zero-mode magnitude is used to identify the fault section in hybrid overhead lines. The method also considers the effect of TW reflections due to adjacent lines in the fault section identification, so it is very versatile, but it does not identify the exact position of the faults. In [28], the change-points caused by the superposition of forward TWs and backward TWs combined with TW arrival time and polarity are used to identify the fault position. The proposed method is very promising and it has been applied to multi-terminal OHL with very good results, but the situation of faults in branched OHL has not been discussed in depth.

In [29], a novel solution to identify reflected waves to locate the fault position is presented, by means of speeded-up robust features. The reflected waves can be effectively separated by dividing them into two inconsistent time windows *i.e.*, the initial wave and the reflected one, so that the first singularity in each time window can be considered to be a traveling wave front. The method proved to be robust and it has been applied to lines with a complex topology. Since the method is based on speeded-up robust feature, it is quite complex to be applied in practice.

C. CONTRIBUTION

From the literature analysis, it emerges that the majority of contributions which exploit single-ended approaches to estimate the fault position in OHLs consider line configurations which are very simple. Nevertheless, there are several TW reflections which can interfere with the fault location and which are strictly related to the line configuration (in practical application, they are more complex than a simple two-terminal structure). Hence, it is important to also analyze more complex line topologies.

In fact, the main difference between the proposed approach and the TWB methods in literature is the possibility of recognizing and erasing the TW reflections related to the grid configuration. In particular, it is possible to erase the TW reflections due to:

- the frequent changes of the tower structure along the line route;
- the presence of lines in parallel with the monitored one;
- the TW reflections coming from other lines starting from the same bus of the monitored one;
- the TW reflections coming from line branches.

From the other hand, the presented approach is relatively simple to implement since it does not require the knowledge of the TW polarities and propagation velocities. In fact, this method decouples the propagation mode from the knowledge the TW propagation velocities, by unlocking the limitation fixed by this dependence, so allowing the study of more complex network configurations. Moreover, additional algorithms to process the fault current signals are not required, differently from some of the TWB methods presented in literature to analyze complex network configurations, to the best of the author knowledge. The present fault location method has been developed for phase-to-ground faults since they are the vast majority of the fault cases in OHLs, and the most difficult to detect in unearthed-operated OHL networks due to the very low current magnitude. The proposed method is based on the observation of the lattice diagram of the line, so it is quite easy to implement. Moreover, its accuracy is improved by the combination of the results obtained by the three-mode propagation analysis. The developed approach is tested on a real network model in the EMTP-RV simulation environment for several phase-to-ground faults along the monitored line. Table 1 summarizes the main features of the proposed method compared to some of the existing fault location methods in literature.

TABLE 1. Comparative table highlighting the contribution of the proposed method compared to the existing literature.

	Impedance based [3-12]	AI based [13-16]	TW based double ended				TW based single ended (applied to simple configurations)		TW based single ended (applied to complex configurations)			
			[18]	[19]	[20]	[21]	[2, 23]	[24-26]	[27]	[28]	[29]	Proposed method
Accuracy independence on neutral connection		✓	✓	✓	✓	✓	✓	✓	✓	✓	✓	✓
Accuracy independence on the fault impedance		✓	✓	✓	✓	✓	✓	✓	✓	✓	✓	✓
Accuracy independence on the TW velocity or polarity	✓	✓		✓	✓	✓		✓	✓		✓	✓
Accuracy independence on software training based on measurement data	✓		✓	✓		✓	✓	✓	✓	✓	✓	✓
One measurement terminal is sufficient for each monitored line	✓						✓	✓	✓	✓	✓	✓
Method tested in lines with a complex configuration		✓							✓	✓	✓	✓
Identification of the fault point (not just the fault branch)	✓	✓	✓	✓	✓	✓	✓	✓		✓	✓	✓
Additional advanced software or algorithm for advanced signal processing is not required	✓	✓	✓	✓	✓	✓	✓	✓	✓	✓		✓

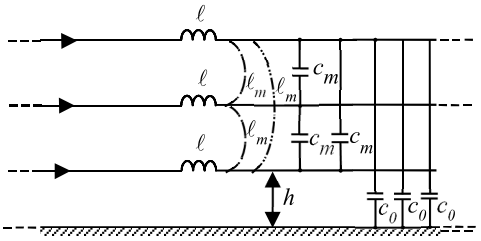

FIGURE 1. Electric model of an Over Head Line (OHL).

II. TW PROPAGATION THEORY

To understand the main hypothesis behind the methodology presented in this paper, it is useful to recall the theory of the TW propagation along an OHL line.

A. RECALLS ON THREE-PHASE TW PROPAGATION ON OHLS

A three-phase non-dissipative model of an OHL characterized by mutual couplings between conductors and between conductors and the ground can be well represented by the three-phase diagram of Fig. 1.

By assuming a symmetrical system without ground wires the time-space relationships between phase currents and voltages can be described by the well-known Heaviside matrix equations [30], [31]:

$$-\frac{\partial}{\partial x}\begin{bmatrix} u_1 \\ u_2 \\ u_3 \end{bmatrix} = \begin{bmatrix} \ell & \ell_m & \ell_m \\ \ell_m & \ell & \ell_m \\ \ell_m & \ell_m & \ell \end{bmatrix} \frac{\partial}{\partial t}\begin{bmatrix} i_1 \\ i_2 \\ i_3 \end{bmatrix} \tag{1}$$

$$-\frac{\partial}{\partial x}\begin{bmatrix} i_1 \\ i_2 \\ i_3 \end{bmatrix} = \begin{bmatrix} c_0+2c_m & -c_m & -c_m \\ -c_m & c_0+2c_m & -c_m \\ -c_m & -c_m & c_0+2c_m \end{bmatrix} \frac{\partial}{\partial t}\begin{bmatrix} u_1 \\ u_2 \\ u_3 \end{bmatrix} \tag{2}$$

where c_0 is the phase to ground capacitance, ℓ is the self-inductance and c_m, ℓ_m are the mutual capacitances and inductances between conductors, respectively. Equations (1) and (2) can be written in a compact form as:

$$-\frac{\partial}{\partial x}\boldsymbol{u_p} = \mathrm{L}\frac{\partial}{\partial t}\boldsymbol{i_p} \tag{3}$$

$$-\frac{\partial}{\partial x}\boldsymbol{i_p} = \mathrm{C}\frac{\partial}{\partial t}\boldsymbol{u_p} \tag{4}$$

where $\boldsymbol{i_p}$ and $\boldsymbol{v_p}$ are 3×1 vectors of current and voltage phase components and $\mathbf{L}$ and $\mathbf{C}$ are 3×3 matrices of phase inductances and capacitances, respectively.

A convenient transformation can be introduced to study the system by means of three independent modes. Different transformation matrices are used for phase to mode transformation (e.g. Karrenbauer, Clarke, Wedepohl) in TW applications [32], [33]. In this study, the Karrenbauer matrix is exploited so the modal currents and voltages can be written as a function of phase currents and voltages as follows:

$$\boldsymbol{i}_m = \mathbf{T}\boldsymbol{i_p}, \boldsymbol{u_m} = \mathbf{T}\boldsymbol{u_p} \tag{5}$$

where $\boldsymbol{i_m}$ and $\boldsymbol{u_m}$ are 3×1 vectors of current and voltage modal components (named *earth mode* 0 *aerial mode* α and *aerial mode* β) and $\mathbf{T}$ is the Karrenbauer matrix, which is expressed by:

$$\mathbf{T} = \frac{1}{3}\begin{bmatrix} 1 & 1 & 1 \\ 1 & -1 & 0 \\ 1 & 0 & -1 \end{bmatrix} \tag{6}$$

Equations (3) and (4) can then be expressed as a function of modal components as follows:

$$-\frac{\partial}{\partial x}u_m = \mathbf{TLT}^{-1}\frac{\partial}{\partial t}\boldsymbol{i}_m \tag{7}$$

$$-\frac{\partial}{\partial x}i_m = \mathbf{TCT}^{-1}\frac{\partial}{\partial t}\boldsymbol{u}_m. \tag{8}$$

Given the structure of $\mathbf{R}$, $\mathbf{L}$ and $\mathbf{C}$ which reflects the perfect symmetry of the studied system, the modal matrices $\mathbf{L_m}$ and $\mathbf{C_m}$ can be derived as follows:

$$\mathbf{L_m} = \mathbf{TLT}^{-1} = \begin{bmatrix} \ell+2\ell_m & 0 & 0 \\ 0 & \ell-\ell_m & 0 \\ 0 & 0 & \ell-\ell_m \end{bmatrix} = \begin{bmatrix} \ell_0 & 0 & 0 \\ 0 & \ell_\alpha & 0 \\ 0 & 0 & \ell_\beta \end{bmatrix} \tag{9}$$

$$\mathbf{C_m} = \mathbf{TCT}^{-1} = \begin{bmatrix} c_0 & 0 & 0 \\ 0 & c+3c_m & 0 \\ 0 & 0 & c+3c_m \end{bmatrix} = \begin{bmatrix} c_0 & 0 & 0 \\ 0 & c_\alpha & 0 \\ 0 & 0 & c_\beta \end{bmatrix} \tag{10}$$

From (9)-(10) it can be recognized that exists a perfect equivalence between modal transformation and sequence transformation for electrical line parameters calculation. In fact, the modal inductances ℓ_0, ℓ_α and ℓ_β are equivalent to the zero-sequence, positive sequence and negative sequence inductances, respectively. The same equivalences are valid for sequence and modal capacitances.

The transformation matrix allows identifying the three decoupled propagation equations, described by (7) and (8), whose integration yields the well-known equations of the TW along a conductive medium, not reported here for the sake of brevity [34] (a solution was obtained by D'Alembelt).

As a consequence of a transient event (phase-to-ground fault, energization, load insertion etc..), voltage and current TWs are generated from the section of interest and propagate through the line in both directions, as long as they find a discontinuity like the substation transformer, a different branch or the fault point (i.e. whenever a different surge impedance is present). A discontinuity point generates a transmitted waves and a reflected wave, with different amplitude depending on the surge impedance of the branches connected to the discontinuity point [35].

B. WAVE PROPAGATION SPEED OF MODAL COMPONENTS

In the case of the ideal system described above, the propagation speeds of TWs along the medium can be derived, for each propagation mode, as follows:

$$v_0 = \frac{1}{\sqrt{\ell_0 c_0}} v_\alpha = \frac{1}{\sqrt{\ell_\alpha c_\alpha}} v_\beta = \frac{1}{\sqrt{\ell_\beta c_\beta}} \tag{11}$$

For a non-dissipative system, the speeds of the three propagation modes along a OHL are identical and equal to the speed of light c, leading to the relation $v_0 = v_\alpha = v_\beta = c$ [36].

Differently, in a real three-phase system, it is necessary to consider the attenuation of the TWs due to the resistive behavior. In particular, in such condition the wave speed is less than c and it is not constant over the time because of the different attenuation of the frequency components of the wave front caused by the skin effect in the conductors and in the ground [37]. In such conditions, components of the signal characterized by higher frequencies, damp faster than those characterized by lower frequencies. This determines a flattening of the wave front over the time. The main consequence of this property is that the wave velocity of the entire current signal changes as a function of time. In particular, by hypothesizing a homogeneous line, the wave speed value monotonically decreases when the TW propagates along the line.

Since the skin effect on the conductor is negligible compared to the one on the ground path, the speed propagation of the *aerial modes* α and β can be assumed to be unchanged and equal to the speed of light c. Otherwise, the speed propagation of the *earth mode* component is more affected by this attenuation since its current path involves the ground resistivity.

Some of the authors, in [2], proposed a methodology to compute the *earth mode* propagation speed by considering the ground return path. By applying the Continuous Wavelet Transform (CWT) [38] on the *earth mode* current, it is possible to compute the wave speed of each frequency component by selecting the proper spectral component of the entire transient signal. The wave speed is constant for the chosen frequency component, excluding small variations in the discontinuity points. The wave speed for the *earth mode* frequency component f^* can be obtained by the following equation:

$$v_0 = \frac{\omega^*}{k_0''} \tag{12}$$

where $\omega^* = 2\pi f^*$ and k_0'' is the imaginary part of the propagation constant $\underline{k}$:

$$\underline{k}_0 = k_0' + jk_0'' = \sqrt{(r_0 + j\omega^* \ell_0)(g_0 + j\omega^* c_0)} \tag{13}$$

where the parameters r_0, ℓ_0, g_0 and c_0 are related to the zero sequence (for the considerations made above) and consider the resistive behavior of the ground return.

By neglecting g_0, which is typically very small, especially for OHL lines, it is possible to demonstrate that for frequencies higher than 10 kHz the zero sequence parameters can be expressed by [39]:

$$r_0 \cong 1.35 \frac{\sqrt{f^* \rho_{soil}}}{h_a} \tag{14}$$

$$\ell_0 \cong 1.38 \log_{10}\left(\frac{4h_a}{d_{eq}}\right) + \frac{210}{h_a}\sqrt{\frac{\rho_{soil}}{f^*}} \tag{15}$$

$$c_0 \cong \frac{24}{3} \frac{1}{\log_{10}\left(\frac{4h_a}{d_{eq}}\right)} \tag{16}$$

where ρ_{soil} is the ground resistivity, d_{eq} is the equivalent diameter of phase conductors while h_a is the average height of conductors from the ground. The formulation (12) has been applied in [2], for fault distance estimation purposes, to compute the speed propagation of the earth mode on real OHL at different frequencies. Nevertheless, the limitation of this formulation is linked to its dependence on the geometrical disposition of the monitored line and, for this reason, it is accurate for simple OHL configurations. In fact, when other adjacent OHLs are considered in the analysis and when the OHL under analysis presents different phase disposition and different heights along its path, the propagation speed assumes multiple values. In this case, a fault location method based on the lattice diagram in unable to choose a-priori the speed associated to each TW reflection.

C. EARTH-MODE PROPAGATION SPEED AT HIGH FREQUENCY

This paper proposes to overcome the limitations introduced by the earth-mode propagation speed, in order to implement an algorithm which can be totally independent of the propagation speed. With this aim, it is interesting to focus

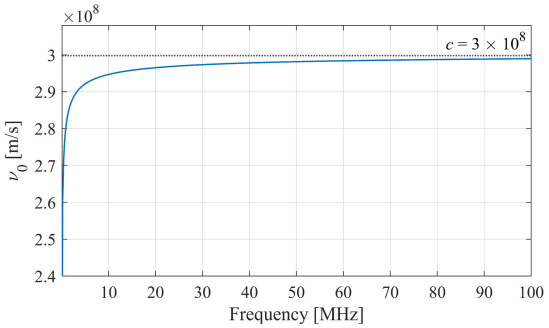

FIGURE 2. Speed propagation of the earth mode as a function of frequency.

on the formulation (12) and to study its dependence on the frequency. In particular, the purpose is to derive the limit of (12) when frequency tends to infinite:

$$\lim_{f\to\infty} \frac{2\pi f}{\text{imag}\left(\sqrt{(r_0 + j2\pi f \ell_0) j2\pi f c_0}\right)} = \frac{1}{\sqrt{l_0 c_0}} = c \quad (17)$$

The step-by step solution of the limit is reported in Appendix A. The result of (17) shows that, when the frequency tends to infinite, the speed propagation of the earth mode for a dissipative system tends to the speed of light (as for the case of non-dissipative system). In Fig. 2, the propagation speed of the earth mode component v_0 is computed by increasing the frequency up to tens of MHz, considering a standard OHLs of an Italian 60 kV grid. The result shows that, with the increasing of the frequency, the propagation speed approaches the speed of light c.

This consideration enables to use the speed of light as the reference speed for *every* modal component, without losing accuracy, whether the frequency component selected for the TW analysis is sufficiently high, e.g., the highest recorded by the instrument. Practically speaking, since the modern devices used for detecting TWs can reach about 10 MHz of sample rate, the approximation of (17) introduces an error of about 1.5 % in the fault distance estimation.

This consideration, together with the ones discussed in Section II-C, are exploited to implement a new fault location method based on TW identification which can deal with big network complexities.

III. NEW TRAVELING WAVE MATRIX IDENTIFICATION METHOD (TWMI)

The purpose of the new methodology, called Traveling Wave Matrix Identification (TWMI) method, is to determine the distance of a single-phase fault occurred along a HV unearthed-operated OHL with a derived branch, from a *single-ended device* equipped with a Traveling Wave Detector (TWD).

The method also allows to consider the presence of other OHLs connected to the same bus where the TWD is connected and the discontinuities in the geometrical phase disposition along the monitored line. The most general single line diagram of the network under analysis is shown in Fig. 3.

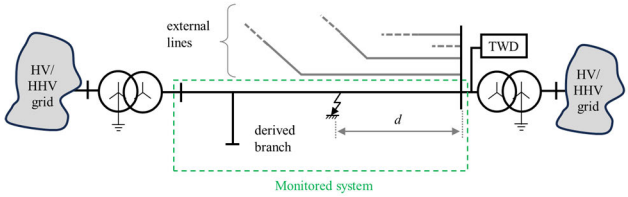

FIGURE 3. Single line diagram of the network under analysis.

A. WAVELET TRANSFORM AND SCALE SELECTION

After the fault occurrence, the TWD records the three phase currents i_a, i_b and i_c with a sample rate of 10 MHz. The adopted sample rate is not related to the present fault location method for itself, but to the model complexity of the EMTP-RV environment. In fact, the simulation environment requires an integration step which is lower than the propagation constant of the line model. In the specific case, due to the model complexity, the minimum required integration step to have the electromagnetic model convergence is equal to 10 MHz. The three signals are processed by applying the modal transformation in (5) and then the CWT, similarly to what has been done in [2].

The CWT acts as a filter for specific frequency component of the signal and it is extremely useful to isolate the reflected and transmitted TWs originated from the fault section [38].

Based on the considerations expounded above about the earth-mode propagation speed, the new methodology, differently from [2], extracts the lowest possible scales of the CWT in which the propagation phenomenon is still detectable (it has been verified that, for very low scales, no reflections can be distinguished). In this study, the adopted mother wavelet is based on the *symlet 2* function, which is largely used for CWT-based TW fault location methods [2], [40], [41]. The choice of this mother wavelet has been confirmed also by several tests, since it has been observed that it fits better with our approach, probably because the *symlet 2* shape is very similar to the transient fault current waveform. Nevertheless, in Section IV, the results are presented also for different mother wavelets.

In order to identify the fastest phenomena, the CWT is applied in cascade to filter the modal components until only the higher frequencies remain. The output signals of these processes are used to select the reflection peaks (as expounded in the next session). Fig. 4 shows the transformations and the filtering process applied to the initial signals $\boldsymbol{i_p}(t)$. In Fig. 4, $\gamma(s, \tau)$ are the CWTs of the signals $\boldsymbol{i_m}(t)$, s is the scale factor, τ is the shifting factor and ψ^* is the complex conjugate of the chosen mother wavelet. The coefficients s_I, s_{II}, s_{III} are the scales used for the three CWT filtering steps and they have to be tuned for the line under analysis.

B. TW PEAK SELECTION: ELIMINATION OF EXTERNAL REFLECTIONS

The signal $\mathbf{III_m}(t)$ obtained by the CWT scale selection process is then processed to extract the TW reflection peaks useful to identify the fault distance.

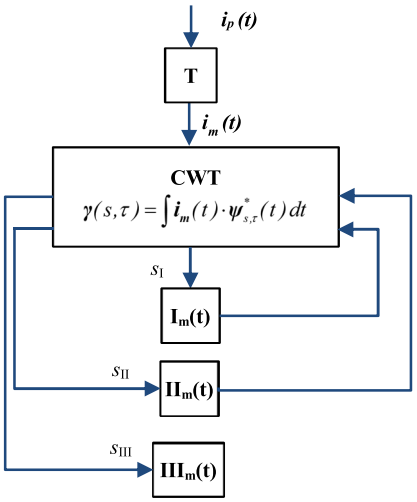

FIGURE 4. Flow chart for the wavelet scale selection.

The first step is the identification of the peaks associated to reflections of TW originated from the fault section and reflected by external line sections, out of the monitored line.

If a fault occurs in the monitored line, the TW reflected by external lines (connected to the same node where the TWD is installed) are originated by the first TW transmitted at the instant t_0 (see Fig.5).

For this reason, the time instant related to the reflection of a TW coming from external lines can be computed by knowing the time instant of the first reflection peak detected by the TWD and the propagation speed, by the following expression:

$$t_{ext} = t_0 + \frac{2L_{ext}}{v_0} \tag{18}$$

where t_0 [s] is the arrival time of the first reflection detected by the TWD, L_{ext} [m] is the length of the external line and v_0 is the propagation speed, equal to the speed of light.

This procedure can be similarly applied for all the lines out of the monitored one.

The identification of the t_{ext} time instants associated to an external line or to the discontinuity along the line allows finding the corresponding peaks of the signal $\mathbf{III_m}(t)$ to be ignored by the signal processing described in the reminder of this section. The peak elimination process is performed within a tolerance band of $\pm\,\varepsilon_{\text{ext}}$ around the t_{ext} instant.

C. TW PEAK SELECTION: IDENTIFICATION OF PEAKS OF INTEREST

The increase in complexity of the grid around the monitored line, together with the presence of mutual coupled line portions, the presence of derived branches and the presence of discontinuities along the line make the exploitation of the classical criteria based on the peak energy content or the peak polarity to identify the fault distance in a single-ended scheme quite difficult to apply.

For this reason, this paper introduces a different fault distance identification criterion based on the knowledge of the topology of the grid. In fact, the presence of discontinuities

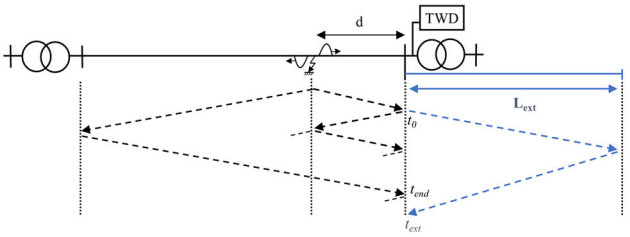

FIGURE 5. Scheme illustrating the identification of external reflections.

modifies the surge impedance of the line generating a reflected and a transmitted wave.

By exploiting this physical phenomenon, the method considers all the possible reflections of the TWs for each discontinuity present along the line (therefore not only from the fault and from the ends of the line) and through a comparative analysis identifies the correct peaks to compute the fault distance.

To physically understand the methodology, refer to the diagram in Fig. 6 where, for illustrative purposes, three discontinuities along the line are considered, namely *dis1, dis2, dis3* in Fig. 6.

The two peaks corresponding to the time instants highlighted in black (t_1 and t_{end}) are those traditionally considered for the calculation of the fault distance and allow the correct estimation of the distance via the well-known (19) and (20):

$$d_1 = \frac{(t_1 - t_0)v_0}{2} \tag{19}$$

$$d_{end} = L_{end} - \frac{(t_{end} - t_0)v_0}{2} \tag{20}$$

The other peaks that reach the TWD at times $t^{+}_{\text{dis}(1)}$, $t^{-}_{\text{dis}(2)}$ and $t^{-}_{\text{dis}(3)}$ originate from reflections coming from discontinuities along the line. Similarly to what is done above in (19) and (20), it is possible to associate each peak with the relative time instant. In particular, two cases can be identified based on the position of the discontinuity with respect to the fault section. If the discontinuity is located after the fault section (e.g. $L_{dis(2)}$ and $L_{dis(3)}$), the expression that returns the correct distance is given by (21), similarly to (20):

$$d_{n-} = L_{dis(j)} - \frac{(t^{-}_{dis(j)} - t_0)v_0}{2} \tag{21}$$

where L_{dis} is the distance between the TWD and the discontinuity.

Otherwise, if the discontinuity is located before the fault section, the expression that returns the correct distance is given by (22):

$$d_{n+} = L_{dis(j)} + \frac{(t^{+}_{dis(j)} - t_0)v_0}{2} \tag{22}$$

Ideally, each peak recorded by the TWD is related to a different formula between (19)-(22), but since the fault distance and therefore the real arrival sequence of the peaks is not known a priori, the method applies simultaneously each formula to each peak time instant, starting from the second

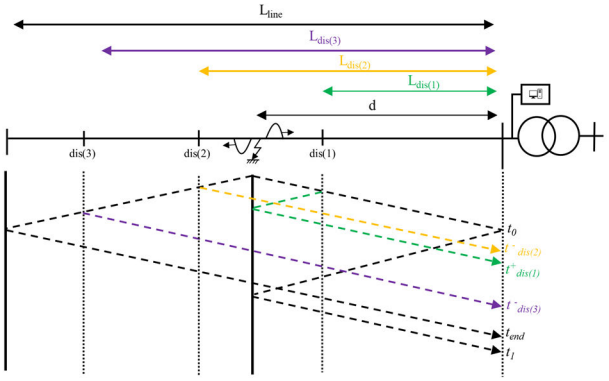

FIGURE 6. Lattice diagram of a line considering the reflections from the points of discontinuity.

peak recorded by the TWD (the first peak recorded is for sure the one coming from the fault section). With this assumption, for a line with n_{dis} internal discontinuities and m_{dir} derived branches, the system of equations to be considered is:

$$\begin{cases} d_1 = \dfrac{(t_x - t_0)v_0}{2} \\ d_{n-} = L_{dis(n)} - \dfrac{(t_x - t_0)v_0}{2} \\ d_{n+} = L_{dis(n)} + \dfrac{(t_x - t_0)v_0}{2} \\ d_m = L_{dir(m)} - \dfrac{(t_x - t_0)v_0}{2} \\ d_{end} = L - \dfrac{(t_x - t_0)v_0}{2} \end{cases} \tag{23}$$

where $x \in \{1,\ldots,2n_{\text{dis}}+3m_{\text{dir}}+2\}$, $n \in \{1,\ldots,n_{\text{dis}}+m_{\text{dir}}\}$ and $m \in \{1,\ldots,m_{\text{dir}}\}$. Therefore, the total number of formulations to apply is $n_{\text{tot}} = 2n_{\text{dis}}+3m_{\text{dir}}+2$ and the number of peaks to extract from the recorded signal is $n_{\text{peaks}} = n_{\text{tot}}+1$.

The first n_{peaks} peaks are selected from the signal $\mathbf{III_m}(t)$ in order of amplitude, from the largest to the smallest one. Then, each formula of the system (23) is applied to each time instant related to the selected peaks except for the first one (the first peak detected corresponds to t_0 and it is used as a reference for the application of (23)).

The result of this application is a $n_{\text{tot}} \times n_{\text{tot}}$ matrix indicated as fault distance matrix **G** in the following. The structure of this matrix is represented in Fig. 7, for a line with $n_{\text{dis}} = 2$ and $m_{\text{dir}} = 1$. Each column represents the application of a different formula of (23).

Each row refers to a time difference between the first peak arrival time t_0 and the arrival time of the other peaks selected by the algorithm, ordered from top to bottom from the most energetic peak to the lowest one.

It is worth noting that the peaks whose amplitude is below a certain threshold compared to the amplitude of the first peak detected are not considered by the algorithm.

For this reason, in some cases it is possible that the rows of **G** are less then n_{tot}, depending on the case under analysis. The threshold parameter for this elimination process is called γ_{lim}.

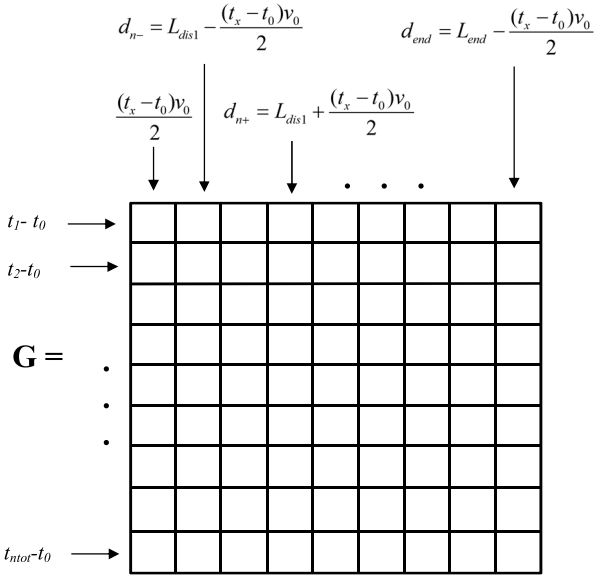

FIGURE 7. Construction of the fault distance matrix G.

D. SEARCHING THE FAULT DISTANCE BEFORE THE DERIVED BRANCH

The matrix **G** contains $n_{tot} \times n_{tot}$ numeric values in units of length. In cases where one of the expressions of (23) related to column j is applied to the time difference in row i corresponding to the correct peak of the lattice diagram, the correct fault distance is found in element (i, j). Therefore, if the first n_{tot} most energetic peaks recorded after the first are actually related to the formulas reported in (23), in each column of the matrix there would be an element that corresponds to the correct fault distance.

This does not always happen in practice, since, depending on where the fault is located along the line, peaks may arrive at the terminal from multiple reflections of other peaks which do not necessarily correspond to one formula of (23).

However, it happens that there are elements of the matrix with similar values in different columns, up to a certain tolerance. Among these repeated elements, there is certainly the correct fault distance.

The algorithm searches the matches among all the elements of the matrix in different columns of the matrix, setting a tolerance ε_{corr}. From the matching search, the following empirically defined criteria may be applied by the algorithm:

- **A**: there are at least *three* correspondences in **G** for a single distance: the fault distance is given by the average of the distances identified by the matching search;
- **B**: there are at least *three* correspondences in **G** but for several distances different from each other: the distance is determined by means of a logic called BESTDIR which exploits the distances between two points of discontinuity, detailed in Appendix B (method **B1**). If BESTDIR is not successful, the algorithm chooses among the distances the ones whose matching values are closest to the **G**(1,1) element, *i. e.* those that consider more energetic peaks close to the TWD. If this

last check indicates multiple distances, the algorithm identifies these distances as possible candidates (method **B2**);

- **C**: there are *two or less* correspondences in **G** for a single distance or for multiple distances different from each other: the BESTDIR algorithm is used (method **C1**); if BESTDIR is not successful, the method chooses among the distances the ones whose correspondences are closest to the element **G**(1,1). If this last check indicates multiple distances, the algorithm identifies these distances as possible candidates (method **C2**);
- **D**: there are *no* correspondences in **G**: the fault distance is given by the element **G**(1,1) *i.e.* by the most energetic peak considered as coming from the first reflection from the fault.

The flow chart in Fig. 8 summarizes the above-mentioned cases and the operating logic of the method, starting from the signals $\mathbf{III_m}(t)$. The procedure is applied in parallel for each of the three modal components so to obtain three fault distance values.

The final fault position is estimated by combining the three results as shown in Section IV.

The parameters used to build the flow diagram indicate respectively:

- $\boldsymbol{D}_{\text{opt}}$: vector containing the distances with multiple matches within the matrix **G** with tolerance $\varepsilon_{\text{corr}}$;
- $\boldsymbol{K}$ vector containing the number of repetitions for each distance in $\mathbf{D}_{\text{opt}}$;
- n_{Dopt}: number of different distances with the same number of repetitions within the matrix **G**;
- D_{fault} fault distance;
- *BestDir*: fault distance identified by the BESTDIR function.

The procedure here reported does not cover the case where the fault occurs after the derived branch. This specific case is covered in the following paragraph and is represented in the flow chart of Fig. 8 with the box *"…searching fault after the derived branch."*

E. SEARCHING THE FAULT DISTANCE AFTER THE DERIVED BRANCH

The fault identification after the derived branch needs a customized procedure since, when the fault occurs far from the TWD, the number of reflections increases and the methods above described sometimes return wrong results.

Take as a reference the lattice diagram in Fig. 9, related to a fault occurring after the derived branch.

The TW that originates from the fault, as well as being transmitted along the entire line and reaching the measurement terminal at time t_0, is reflected from the point of line branching and generates another wave which in turn is reflected at the derived branch end and reaches the TWD at time $t_{\text{dir}(1)}$. Also, multiple reflections from the branch end can arrive to the TWD at time $t_{\text{dir}(k)}$. The difference between the arrival times of the two peaks recorded by the TWD, if used

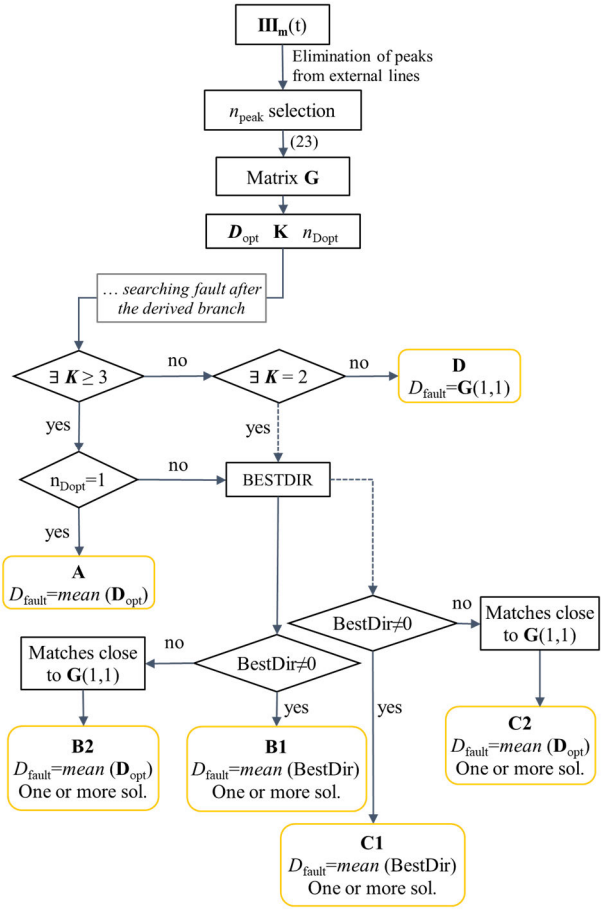

FIGURE 8. Flow chart summarizing the TWMI.

to calculate the fault distance with the usual formula (24), returns the exact length of the branch:

$$L_{dir} = \frac{(t_{dir(k)} - t_0)v_0}{2} \tag{24}$$

Since L_{dir} is known, it is possible to identify the peaks reflected from the branch end directly from the fault matrix **G** and in particular from the first column of the matrix, where the distances computed with (24) (formally equal to (19)) are located. The distance is identified within a certain tolerance ε_{dir}, so the condition for the peak selection within the G matrix is given by:

$$\left|\mathbf{g}_{\mathbf{p},1} - \mathbf{k} \cdot L_{dir}\right| < \varepsilon_{dir} \tag{25}$$

where $\mathbf{g}_{\text{p},1}$ is the first column of **G** and **k** is a vector whose dimension is the number of multiple reflections from the derived-end branch. If exist elements of $\mathbf{g}_{\text{p},1}$ satisfying (25), *i.e.* $\mathbf{g}_{\text{p(k)},1}$, the algorithm recognizes that the fault occurred after the derived branch.

Then, the correct fault distance is identified from the elements of the last column of **G**, for which the formula computing the peaks as coming from the end-of-line reflection is used. This assumption can be adopted since it is very likely that the most energetic peaks recorded by the TWD in case

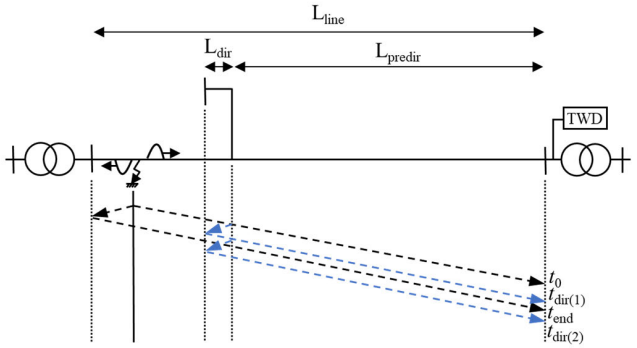

FIGURE 9. Lattice diagram for a fault after the derived branch.

of faults far from the terminal are precisely those relating to a reflection from the end of the line.

This observation arises from the fact that, when a fault is located near the end-of-line terminal, the TW originated from the fault point and reflected by the end-of-line are the first to arrive at the TWD without further attenuations caused by possible multiple reflections and therefore they present a high energy content.

The element of the last column identifying the fault distance is the element just after the row where the elements of $\mathbf{g}_{p(k),1}$ have been detected. Fig. 10 shows the flow diagram that summarizes the procedure to locate the fault after the derived branch. In the flow chart, id1=min(**p**– {p1}) and idk = min(**p**– {**p**(**k**)}), where **p** is the vector containing the indexes of the elements of the last column of **G**, p1 is the row index of the element $g_{p(1),1}$ and **p**(**k**) are the row indexes of the elements $\mathbf{g}_{p(k),1}$.

The flow chart of Fig. 8 shows how the general method presented in section III-D integrates this new procedure. In fact, if conditions (1) of Fig. 9 is not satisfied, the algorithm skip after the block "*...searching fault after the derived branch.*"

IV. SIMULATION RESULTS

With the aim of testing the performance of the implemented algorithm, the model of a real system is implemented in the simulation environment EMTP-RV. Several faults are simulated and the recorded currents are used as an input for the TWMI algorithm.

The analyzed system is a portion of unearthed 50 kV network located in Northern Italy, made up of the monitored OHL and other OHLs connected to the bus where the TWD is placed.

The model implemented in EMTP-RV is depicted in Fig. 11. A single line diagram of the system under analysis is shown in Fig. 12. The monitored line (in black in Fig. 12, from Bus 1 to Bus 2) presents one derived branch (L_{dir}) and four different line stretches along its main path, each of them characterized by a different tower top structure. Along the stretch T1 the OHL is electromagnetically coupled with another OHL installed on the same tower.

The detailed features of the monitored OHL are resumed in Tab. 2 and the global features of the network are reported

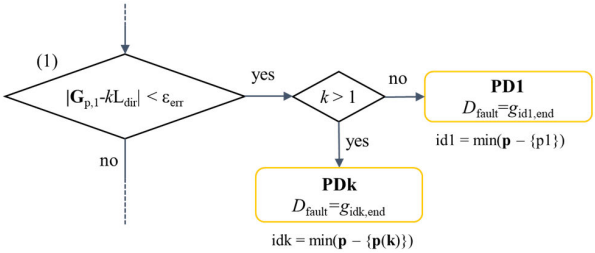

FIGURE 10. Flow chart of the fault distance search after the derived branch.

in Tab. 3. The load supplied by the derived branch of the monitored OHL is set to $\underline{S}_{load}$ =5 MW + j1 Mvar. The stray capacitances of TR1, which have a non-negligible impact on the earth-mode current behavior during the fault transient, are modelled according to the considerations made by some of the authors in [42].

Table 4 resumes the settings of the TWMI algorithm adopted for the simulation presented in this section. A total of twenty phase-to-ground faults has been simulated, ten of which before the derived branch and the remainder after it. The behaviors of the three phase currents flowing in the Bus 1 are processed by the TWMI algorithm following the fault event. The simulation has been performed by means of a computer with a Intel(R) Core (TM) i7-7700K CPU @ 4.20 GHZ processor and with 32 GB of RAM. The mean CPU time to run each simulation for a single fault is 0.25 s.

Table 5 resumes the fault distances resulting from the analysis of the three modal components for the faults before the derived branch. The errors obtained for the faults before the derived branches are, for each fault, far below 1%, with a maximum absolute error of 32 m (for the fault at 3.63 km).

As shown in Tab. 5, the analyzes of the three modes not necessarily use the same TWMI criterion but reaches the same results. This demonstrates the effectiveness of the proposed identification approach.

The analysis of the Beta mode, in average, is the one that return the best results.

For faults close to the TWD, the algorithm is weaker and, in some cases, returns two different possible solutions (for the alpha and earth modes analysis).

Nevertheless, the combination of the three component helps to identify the correct solution.

In order to exemplify the process used by the TWMI to identify the fault, let us take as a reference the fault at 5.03 km. Fig. 13 shows the three-phase current behaviors following the occurrence of the phase-to ground fault.

Fig. 14 shows the earth-mode current resulting from the Karrenbauer transformation.

Fig. 15 shows the signal $\mathbf{III_0}(t)$, resulting from the filtering process of the CWT and the scale selection (refer to Fig. 4). The CWT coefficients (CWC) are weighted on the amplitude of the first peak detected. The peak selected by the algorithm to build the fault matrix are circled in red. Instead, the peak circled in black is excluded by the selection because it derives from a reflection from an external line.

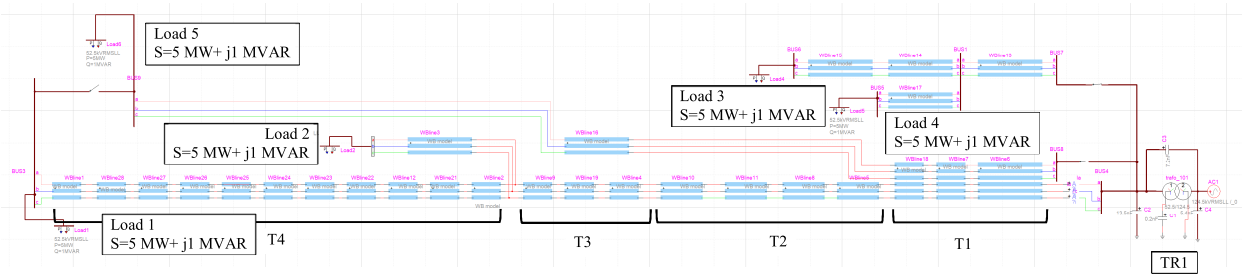

FIGURE 11. EMTP-RV model.

TABLE 2. Detail of the monitored OHLs modelled in EMTP-RV.

	T1	T2	T3	T4	L_{dir}
Length [km]	2.515	.318	2.121	3.624	0.235
ρ_t [Ωm]	1300	1300	1300	1300	1300
Conductor diameter [mm]	14.1	14.1	14.1	15.85	14.1
$r_{20°}$ [Ω/km]	0.257	0.257	0.257	0.22	0.257
Ground wire $r_{20°}$ [Ω/km]	-	-	6.112	3.191	-
Diameter ground wire [mm]	-	-	7.5	10.5	-

TABLE 3. Global features of the network modelled in EMTP-RV.

	L_{line}	$L^{(1)}_{ext}$	$L^{(2)}_{ext}$	$L^{(3)}_{ext}$	TR1	TR2
Voltage [kV]	50	50	50	50	126/ 52.5	52/ 22
From bus	1	1	1	1	-	-
To bus	2	2	4	5	-	-
Length [km]	13.578	12.462	17.596	32.830	-	-

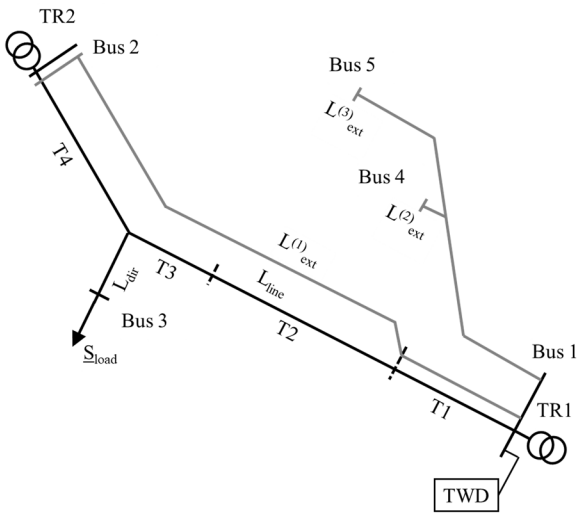

FIGURE 12. Single line diagram of the system modelled in EMTP-RV.

For the sake of brevity, only the fault matrix **G** related to the earth-mode component of the case under analysis is reported in Table 6.

TABLE 4. Setting of the TWMI algorithm.

Par.	Value	Unit	Description
s_I	2	-	Scale of the 1st CWT filtering
s_{II}	2	-	Scale of the 2nd CWT filtering
s_{III}	0.334	-	Scale of the 3rd CWT filtering
τ_{ext}	1	s	Tolerance for external peaks searching
n_{dis}	3	-	Number of discontinuities
m_{dir}	1	-	Number of derived branches
ε_{corr}	25	m	Tolerance for matching searching in **G**
ε_{Bdir}	15	m	Tolerance for BESTDIR algorithm
ε_{dir}	40	m	Tolerance for derived branch searching
γ_{lim}	0.5	%	Threshold for peak elimination
n_{peak}		-	Number of selected peaks

TABLE 5. Results of TWMI for 10 phase-to-ground faults before the derived branch based on the three modal components.

Fault [km]	Earth mode [km]	Beta mode [km]	Alpha mode [km]	TWMI Method	Error [%]*
0.62	0.62/1.90	0.62	1.91	C2/C2/D	0.02
1.62	0.90/1.62	1.63	0.9/1.61	C2/D/B2	0.05
2.52	2.53	2.48	2.48	D/A/B1	0.20
3.63	3.66	3.59	2.53	D/B1/D	0.24
5.03	5.05	5.04	5.05	A/A/A	0.10
6.43	6.43	6.43	6.43	B1/A/A	0.04
7.83	7.81	7.81	7.8	A/A/A	0.19
8.54	8.54	8.52	8.54	A/A/A	0.05
9.25	9.23	9.24	9.23	C1/A/A	0.09
9.95	9.95	9.97	9.95	A/A/A	0.05

*Percentage error computed with respect to the total length of the monitored line, obtained by computing the average of the results related to the propagation modes giving similar distances.

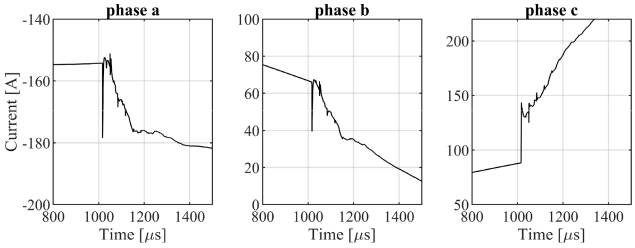

FIGURE 13. Simulated current following the fault at 5.03 km.

The empty spaces are negative values or values greater than the monitored line length, so they are automatically deleted by the TWMI algorithm. The green cells are the matching distances identified by the algorithm.

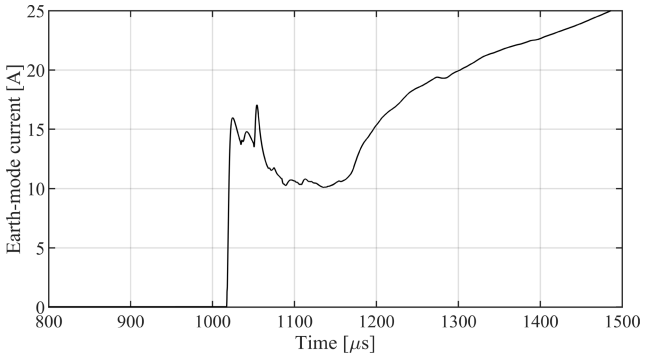

FIGURE 14. Earth-mode current related to the fault at 5.03 km.

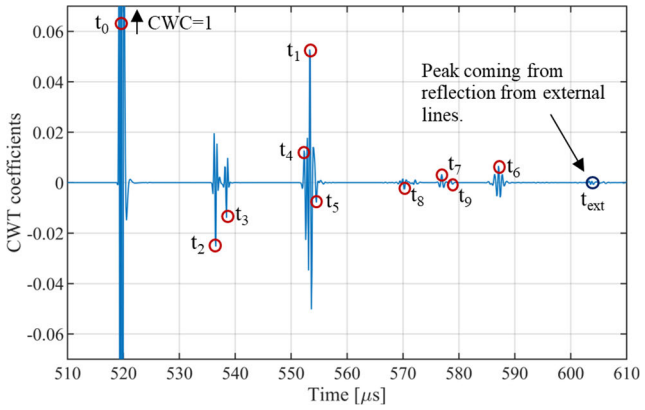

FIGURE 15. CWT coefficients resulting from the CWT filtering process, related to the fault at 5.03 km.

TABLE 6. Fault matrix G of the earth-mode for the fault at 5.033 km.

5.05		2.79	4.91	7.56	12.88	15.00	5.14	8.53
2.53		5.30	7.42	5.05	10.36	12.48	7.66	11.05
2.82		5.02	7.14	5.33	10.65	12.77	7.37	10.76
4.90		2.94	5.06	7.41	12.73	14.85	5.29	8.68
5.23		2.61	4.73	7.74	13.06	15.18	4.96	8.35
10.11				12.62	17.94	20.06	0.08	3.47
8.59			1.37	11.10	16.42	18.54	1.60	4.99
7.58		0.26	2.38	10.09	15.41	17.53	2.61	6.00
10.26				12.77	18.09	20.21		3.32

The algorithm has been tested also by applying different mother wavelets in the CWT scale selection stage. In particular, the algorithm has been tested also for the *Morlet* and for the *Symlet 4* functions. Table 7 shows the output results of TWMI for 10 phase-to-ground faults using *Morlet* as mother wavelet, by analyzing the three-modal components. Table 8 shows the results related to the *Symlet 4* function. The results highlight that, for different mother wavelets, the percentage error increases compared to the results obtained with the *Symlet 2* function, especially for faults close to the measurement terminal and to the line branch. In general, the *Symet 2* is the mother wavelet giving the best results in terms of percentage error for all the analyzed fault cases.

Fig. 16 compares the behavior of the wavelet scale selected by the algorithm for the three mother wavelets. It is possible to see that the *morlet* function is affected by an higher attenuation.

As regards the fault after the derived branch, Table 9 resumes the fault distances resulting from the analysis of the three modal components for the faults after the derived branch. In this case, the algorithm manages to recognize, for each fault, the branch in which the fault occurs.

TABLE 7. Results of TWMI for 10 phase-to-ground faults using "Morlet" as mother wavelet.

Fault [km]	Earth mode [km]	Beta mode [km]	Alpha mode [km]	TWMI Method	Error [%]*
0.62	0.62	0.62/1.89	1.91	C2/C2/D	0.01
1.62	0.90	1.64	0.18	C2/C2/D	5.33
2.52	2.5	0.18	2.50	D/D/C2	0.10
3.63	3.65	3.65	0.18	D/D/D	0.10
5.03	5.05	0.18	5.02	A/D/A	0.11
6.43	2.50	6.43	9.02	C2/A/B1	4.93
7.83	5.71	7.83	7.84	A/A/B1	0.01
8.54	8.53	8.80	8.5	A/A/C1	0.05
9.25	9.26	8.81	8.81	C1/A/A	3.23
9.95	0.24	8.90	8.90	C2/A/A	7.73

*Percentage error computed with respect to the total length of the monitored line, obtained by computing the average of the results related to the propagation modes giving similar distances.

TABLE 8. Results of TWMI for 10 phase-to-ground faults using "symlet4" as mother wavelet.

Fault [km]	Earth mode [km]	Beta mode [km]	Alpha mode [km]	TWMI Method	Error [%]*
0.62	0.63	0.62	0.61/1.91	C2/D/B2	0.01
1.62	8.16	5.80	8.15	C2/A/B1	60.06
2.52	2.53	2.48	2.47	D/A/A	0.10
3.63	3.67	3.55	3.55	D/A/A	0.10
5.03	5.06	5.05	5.05	A/A/A	0.11
6.43	6.42	6.41	6.4	C2/A/A	0.15
7.83	2.12	7.79	4.18	A/B1/B1	34.58
8.54	8.53	8.53	7.10	A/A/B1	0.05
9.25	6.71	9.25	0.707	C1/A/D	40.91
9.95	0.24	9.96	0.225	C2/A/D	71.64

*Percentage error computed with respect to the total length of the monitored line, obtained by computing the average of the results related to the propagation modes giving similar distances.

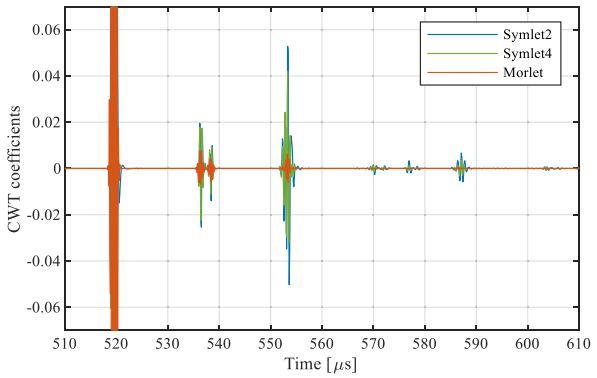

FIGURE 16. Comparison between CWT coefficients for different Mother Wavelets resulting from the CWT filtering process, related to the fault at 5.03 km.

TABLE 9. Results for TWMI for 10 phase-to-ground faults after the derived branch based on the three modal components.

Fault [km]	Earth mode [km]	Beta mode [km]	Alpha mode [km]	TWMI Method	Error [%]*
10.06	10.82	10.04	10.05	PD2/PD2/A	0.16
10.42	10.85	10.40	10.40	PD1/PD1/P1	0.12
10.77	10.85	10.40	10.40	PD1/PD1/P1	2.70
11.12	10.76	12.40	12.40	PD2/PD1/P2	9.46
11.47	12.01	12.06	11.45	PD2/PD1/P2	4.16
11.82	10.81	11.76	11.76	PD2/PD2/P2	0.48
12.17	10.76	12.18	12.18	PD2/PD2/P2	0.03
12.52	12.51	12.51	12.46	PD2/PD1/P2	0.11
12.88	12.87	12.87	12.84	PD2/PD2/PD	0.04
13.23	13.22	13.29	13.17	PD2/PD3/PD2	0.44

*Percentage error computed with respect to the total length of the monitored line, obtained by combining the results related to the propagation modes giving similar distances.

As a first consideration, it can be observed that the results obtained by the earth-mode analysis presents errors on average greater than the one obtained by the other two components. This is probably due to the greater attenuation to which the earth mode component is subjected.

This phenomenon is true in general but becomes non negligible for faults far from the TWD. The combination of the three modes returns, for the most, errors far below 1% also in this case. Only three faults present errors over 1%, and in particular the third fault (2.7 %), the fourth fault (9.46 %) and the fifth fault (4.16 %).

The reason behind these greater errors in these three cases, is that the correct distance is not present in the last column of matrix **G**, but in the column related to the formula which computes the distance based on the point of derivation. Further research is necessary to overcome such loss of accuracy.

However, from the literature analysis [27], [29], it emerges that the maximum errors of single-ended methods applied to OHLs with a complex topology is comparable with these values. Table 7 shows the fault matrix **G** resulting from the analysis of the beta-mode of the fourth fault (at 11.12 km). The red cell of Table 7 is the one automatically extracted by TWMI and the green cell is the correct fault distance. This result suggests that, for faults after the derived branch, in some cases it is necessary to focus not only on the reflections from the end-of-line, which, as observed, do not always generate a TW detectable by the TWD, but on those coming from the point of derivation.

V. CONCLUSION

The paper presents the TWMI method, a novel TW-based methodology which, by means of a single terminal, is able to automatically compute the fault distance in a unearthed operated network with a complex topology, that includes derived branches, line discontinuities and external lines. Authors choose to investigate such operating condition since the small value of the fault current complicates the fault position detection and no methods in literature analyze this scenario in depth. Moreover, the proposed approach is independent of both the TW polarities and propagation speed, making it relatively simpler and more versatile to apply.

TABLE 10. Fault matrix G of the beta-mode for the fault at 11.12 km.

0.24	2.27	7.59	9.71	2.76	8.07	10.20	9.95	13.34
1.17	1.34	6.66	8.78	3.69	9.01	11.13	9.01	12.40
10.02				12.53	17.85	19.97	0.17	3.56
11.18				13.69	19.01	21.13		2.40
10.24				12.76	18.08	20.20		3.33
0.48	2.03	7.35	9.47	3.00	8.32	10.44	9.71	13.10
2.77		5.06	7.18	5.29	10.60	12.73	7.42	10.81
1.42	1.10	6.42	8.54	3.93	9.25	11.37	8.77	12.16
2.35	0.17	5.48	7.60	4.86	10.18	12.30	7.84	11.23

The output of the methodology is the construction of a fault matrix containing, for sure, the correct fault distance. The algorithm is tested on a full flagged EMTP-RV model of a real network, for 20 faults along the monitored line.

The results show that TWMI is able to automatically identify the fault distance for every fault before and after the derived branch with a satisfying accuracy, by means of the combination of the results of different modes of propagation.

Although the results are very encouraging, the present approach still has some limitations that require additional research activity. The first one is related to the adopted sample rate. As mentioned, the minimum integration step to obtain the model convergence is 10 MHz. Although there are measurement devices with such sample rate available in the market, further researches are ongoing to understand if the present approach can work with the same accuracy even with lower sample rates.

A second limitation of the present method is that the faults after a line branch are identified with a lower accuracy compared to the faults before the line branch. Even though in the worst fault case the accuracy of the method is comparable with the one of single-ended methods proposed in literature for complex line topologies, this aspect could be improved in the future. In particular, the carried-out analyzes suggest that, in order to increase the precision of the algorithm, it is necessary to focus, for faults after derived branches, not only on the reflections coming from the end-of-line but also on those coming from the point of derivation.

APPENDIX A

STEP-BY-STEP SOLUTION OF (17)

The limit (17) has a solution in the indeterminate form ∞/∞, in which the order of the numerator n and denominator d functions are the same:

$$\lim_{f\to\infty} \frac{n(f)}{d(f)} \approx \frac{\infty}{\infty} \tag{A1}$$

This suggests that a finite solution is possible. First, it seems convenient to isolate the frequency contribution by

introducing the following expressions:

$$r_a = 1.35\frac{\sqrt{\rho_{soil}}}{h_a},\ \ell_a = 1.38\log_{10}\left(\frac{4h_a}{d_{eq}}\right),\ \ell_b = \frac{210}{h_a}\sqrt{\rho_{soil}}. \tag{A2}$$

The expression of $d(f)$ can thus be written as:

$$d(f) = \text{imag}\left(\sqrt{-4\pi^2 c_0 f^2\left(\ell_a + \frac{\ell_b}{\sqrt{f}}\right) + j2\pi c_0 r_a f\sqrt{f}}\right) \tag{A3}$$

By recalling that the imaginary part of a square root of a complex number, say $z = a+\text{j}b$, can be computed as:

$$\text{imag}\left(\sqrt{z}\right) = \pm\frac{b}{|b|}\sqrt{\frac{|z|-a}{2}}$$

where, in this specific case:

$$a = -4\pi^2 c_0 f^2\left(\ell_a + \frac{\ell_b}{\sqrt{f}}\right)$$
$$b = 2\pi c_0 r_a f\sqrt{f}$$
$$|z| = 2\pi f\sqrt{f}\cdot\sqrt{4\pi^2\left(\ell_a\sqrt{f}+\ell_b\right)^2 + r_a^2}$$

the expression (A3) can be written as:

$$d(f) = \pm\sqrt{\frac{\pi f\sqrt{f}\cdot\sqrt{4\pi^2\left(\ell_a\sqrt{f}+\ell_b\right)^2 + r_a^2} + }{2\pi^2 c_0 f^2\left(\ell_a + \frac{\ell_b}{\sqrt{f}}\right)}} \tag{A4}$$

when f tends to infinite, it is possible to assume that:

$$4\pi^2\left(\ell_a\sqrt{f}+\ell_b\right)^2 + r_a^2 \approx 4\pi^2\left(\ell_a\sqrt{f}+\ell_b\right)^2$$
$$\left(\ell_a\sqrt{f}+\ell_b\right) \approx \ell_a\sqrt{f}$$
$$\left(\ell_a + \frac{\ell_b}{\sqrt{f}}\right) \approx \ell_a$$

so (A4) can be simplified as (by assuming $f > 0$):

$$d(f) \approx \pm\sqrt{4\pi^2 f^2 c_0\ell_a}. \tag{A5}$$

Finally, by recalling the initial limit in (17), it is possible to write:

$$\lim_{f\to\infty}\frac{2\pi f}{\pm 2\pi f\sqrt{c_0\ell_a}} = \frac{1}{\sqrt{c_0\ell_0}} \tag{A6}$$

by only holding the positive solution and by remembering that $\ell_a = \ell_0$.

APPENDIX B
BESTDIR FUNCTION: CALCULATION OF THE FAULT DISTANCE BY EXPLOITING THE REFLECTIONS FROM THE LINE DISCONTINUITIES

As already mentioned, the presence of discontinuities along the line rises reflections of the TWs coming from the fault which reach the TWD at different time instants.

If, on one hand, the presence of these discontinuities increases the complexity in the identification of the fault distance, on the other it can constitute an advantage when interpreting the peaks recorded by the TWD. In fact, if the spatial distances between the discontinuities are known, and thanks to the possibility of using the speed of light as propagation speed, it is possible to convert the spatial information into time-based one, relating the time differences between the arrival of the different peaks at the TWD and the lengths of the homogeneous sections of the line. In particular, considering a homogeneous stretch along the line equal to d_{xy}, the corresponding temporal distance can be computed by (B1) as deduced from the lattice diagram of Fig. 17:

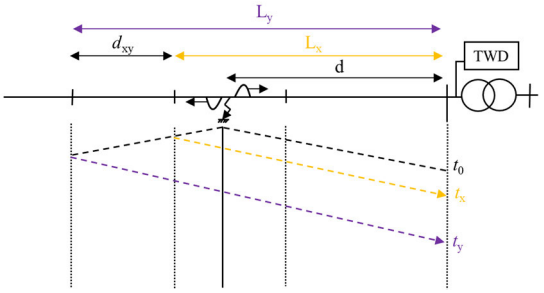

FIGURE 17. Lattice diagram calculating the fault distance from the BESTDIR function.

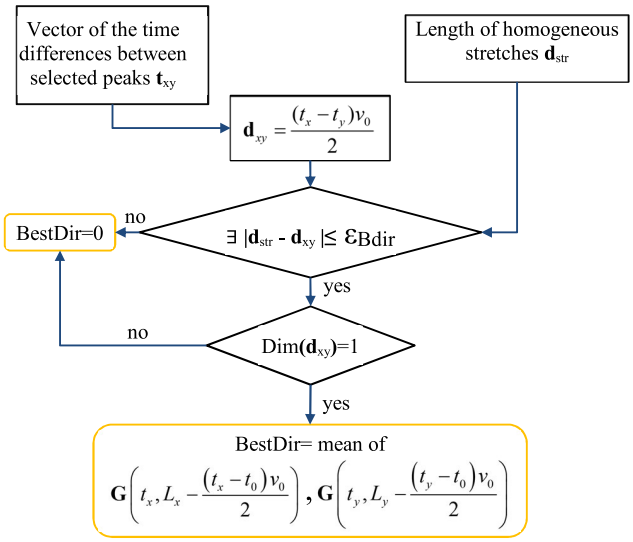

FIGURE 18. Flow chart of the BESTDIR function.

$$d_{xy} = \frac{(t_x - t_y)v_0}{2} \tag{B1}$$

where t_x and t_y are the arrival times of the two peaks originated from the fault and reflected from the starting point and the final point of the homogeneous stretch d_{xy}. The algorithm, therefore, searches among all the selected peaks the presence of time differences compatible with the spatial distances between the discontinuities d_{xy} (with a tolerance ε_{Bdir}). If the search is successful, the fault distance can be calculated as an average of the elements of the matrix $\mathbf{G}$ in the two rows corresponding to the two arrival times t_x and t_y and in the columns related to the two formulas referring to the

initial point and the final point of the homogeneous section. The logic of this function is schematized in the flow chart of Fig. 18.

REFERENCES

[1] E. Papadis and G. Tsatsaronis, "Challenges in the decarbonization of the energy sector," *Energy*, vol. 205, Aug. 2020, Art. no. 118025, doi: 10.1016/j.energy.2020.118025.

[2] R. Benato, S. D. Sessa, M. Poli, C. Quaciari, and G. Rinzo, "An online travelling wave fault location method for unearthed-operated high-voltage overhead line grids," *IEEE Trans. Power Del.*, vol. 33, no. 6, pp. 2776–2785, Dec. 2018, doi: 10.1109/TPWRD.2018.2816067.

[3] M. M. Saha, J. Izykowski, and E. Rosolowski, "Fault location on power networks," in *Power Systems*. London, U.K.: Springer, 2010, doi: 10.1007/978-1-84882-886-5.

[4] S. M. Hashemian, S. N. Hashemian, and M. Gholipour, "Unsynchronized parameter free fault location scheme for hybrid transmission line," *Electr. Power Syst. Res.*, vol. 192, Mar. 2021, Art. no. 106982, doi: 10.1016/j.epsr.2020.106982.

[5] K. Zimmerman and D. Costello, "Impedance-based fault location experience," presented at the IEEE Rural Electric Power Conf., Apr. 2006.

[6] A. Farughian, L. Kumpulainen, and K. Kauhaniemi, "Review of methodologies for Earth fault indication and location in compensated and unearthed MV distribution networks," *Electr. Power Syst. Res.*, vol. 154, pp. 373–380, Jan. 2018, doi: 10.1016/j.epsr.2017.09.006.

[7] L. U. Iurinic, A. R. Herrera-Orozco, R. G. Ferraz, and A. S. Bretas, "Distribution systems high-impedance fault location: A parameter estimation approach," *IEEE Trans. Power Del.*, vol. 31, no. 4, pp. 1806–1814, Aug. 2016, doi: 10.1109/TPWRD.2015.2507541.

[8] M. B. Djurić, Z. M. Radojević, and V. V. Terzija, "Digital signal processing algorithm for arcing faults detection and fault distance calculation on transmission lines," *Int. J. Electr. Power Energy Syst.*, vol. 19, no. 3, pp. 165–170, Mar. 1997, doi: 10.1016/s0142-0615(96)00034-8.

[9] Z. M. Radojevic, V. V. Terzija, and N. B. Djuric, "Numerical algorithm for overhead lines arcing faults detection and distance and directional protection," *IEEE Trans. Power Del.*, vol. 15, no. 1, pp. 31–37, Jan. 2000, doi: 10.1109/61.847225.

[10] D. Novosel, D. Hart, Y. Hu, and J. Myllymaki, "System for locating faults and estimating fault resistance in distribution networks with tapped loads," U.S. Patent 5 839 093 A, Nov. 17, 1998.

[11] S. Hänninen and M. Lehtonen, "Earth fault distance computation with fundamental frequency signals based on measurements in substation supply bay," VTT Tech. Res. Centre Finland, Espoo, Finland, Tech. Rep. VTT-TIED-2153, 2002.

[12] J. Altonen and A. Wahlroos, "Advancement in foundamental frequency impedence based Earth-fault location in unearthed distribution networks," in *Proc. 19th Int. Conf. Electr. Distrib.*, Vienna, Austria, May 2007, p. 4.

[13] J. Thapa, M. Egan, and M. Benidris, "A machine learning-based approach to detection of fault locations in transmission networks," in *Proc. North Amer. Power Symp. (NAPS)*, Oct. 2022, pp. 1–6, doi: 10.1109/NAPS56150.2022.10012184.

[14] H. Mirshekali, R. Dashti, A. Keshavarz, and H. R. Shaker, "Machine learning-based fault location for smart distribution networks equipped with micro-PMU," *Sensors*, vol. 22, no. 3, p. 945, Jan. 2022, doi: 10.3390/s22030945.

[15] C. Zhou, S. Gui, Y. Liu, J. Ma, and H. Wang, "Fault location of distribution network based on back propagation neural network optimization algorithm," *Processes*, vol. 11, no. 7, p. 1947, Jun. 2023, doi: 10.3390/pr11071947.

[16] J. Mora, G. Carrillo, and L. Perez, "Fault location in power distribution systems using ANFIS nets and current patterns," in *Proc. IEEE/PES Transmiss. Distribution Conf. Expo., Latin Amer.*, Aug. 2006, pp. 1–6, doi: 10.1109/TDCLA.2006.311428.

[17] E. O. Schweitzer, A. Guzmán, M. V. Mynam, V. Skendzic, B. Kasztenny, and S. Marx, "Locating faults by the traveling waves they launch," in *Proc. 67th Annu. Conf. Protective Relay Eng.*, Mar. 2014, pp. 95–110, doi: 10.1109/CPRE.2014.6798997.

[18] R. Zeng, Q. Wu, and L. Zhang, "Two-terminal traveling wave fault location based on successive variational mode decomposition and frequency-dependent propagation velocity," *Electr. Power Syst. Res.*, vol. 213, Dec. 2022, Art. no. 108768, doi: 10.1016/j.epsr.2022.108768.

[19] P. O. Kwasi Anane, Q. Huang, O. Bamisile, and P. N. Ayimbire, "Fault location in overhead transmission line: A novel non-contact measurement approach for traveling wave-based scheme," *Int. J. Electr. Power Energy Syst.*, vol. 133, Dec. 2021, Art. no. 107233, doi: 10.1016/j.ijepes.2021.107233.

[20] X. Wang, P. Zhou, X. Peng, Z. Wu, and H. Yuan, "Fault location of transmission line based on CNN-LSTM double-ended combined model," *Energy Rep.*, vol. 8, pp. 781–791, Aug. 2022, doi: 10.1016/j.egyr.2022.02.275.

[21] F. B. Costa, F. V. Lopes, K. M. Silva, K. M. C. Dantas, R. L. S. França, M. M. Leal, and R. L. A. Ribeiro, "Mathematical development of the sampling frequency effects for improving the two-terminal traveling wave-based fault location," *Int. J. Electr. Power Energy Syst.*, vol. 115, Feb. 2020, Art. no. 105502, doi: 10.1016/j.ijepes.2019.105502.

[22] F. V. Lopes, K. M. Dantas, K. M. Silva, and F. B. Costa, "Accurate two-terminal transmission line fault location using traveling waves," *IEEE Trans. Power Del.*, vol. 33, no. 2, pp. 873–880, Apr. 2018, doi: 10.1109/TPWRD.2017.2711262.

[23] D. Rezaei, M. Gholipour, and F. Parvaresh, "A single-ended traveling-wave-based fault location for a hybrid transmission line using detected arrival times and TW's polarity," *Electr. Power Syst. Res.*, vol. 210, Sep. 2022, Art. no. 108058, doi: 10.1016/j.epsr.2022.108058.

[24] H. Shu, D. Duan, and X. Tian, "Single-ended fault location for direct distribution overhead feeders based on characteristic distribution of traveling waves along the line," *Electr. Power Syst. Res.*, vol. 185, Aug. 2020, Art. no. 106345, doi: 10.1016/j.epsr.2020.106345.

[25] F. V. Lopes, E. J. S. Leite Jr., J. P. G. Ribeiro, A. B. Piardi, A. V. Scheid, G. Zat, and R. G. F. Espinoza, "Single-ended multi-method phasor-based approach for optimized fault location on transmission lines," *Electr. Power Syst. Res.*, vol. 212, Nov. 2022, Art. no. 108361, doi: 10.1016/j.epsr.2022.108361.

[26] R. L. A. Reis, F. V. Lopes, W. L. A. Neves, D. Fernandes Jr., C. M. S. Ribeiro, and G. A. Cunha, "An improved single-ended correlation-based fault location technique using traveling waves," *Int. J. Electr. Power Energy Syst.*, vol. 132, Nov. 2021, Art. no. 107167, doi: 10.1016/j.ijepes.2021.107167.

[27] K. Nayak and A. K. Pradhan, "Faulted section identification in mixed lines using one end current traveling waves," *IEEE Syst. J.*, vol. 17, no. 1, pp. 1443–1452, Mar. 2023, doi: 10.1109/JSYST.2022.3184866.

[28] X. Tian and H. Shu, "A new method of single terminal traveling wave location based on characteristic of superposition of forward traveling wave and backward traveling wave," *Int. J. Electr. Power Energy Syst.*, vol. 133, Dec. 2021, Art. no. 107072, doi: 10.1016/j.ijepes.2021.107072.

[29] P. Cao, H. Shu, B. Yang, J. Dong, Y. Fang, and T. Yu, "Speeded-up robust features based single-ended travelling wave fault location: A practical case study in Yunnan power grid of China," *IET Gener., Transmiss. Distrib.*, vol. 12, no. 4, pp. 886–894, Feb. 2018, doi: 10.1049/iet-gtd.2017.0735.

[30] O. Heaviside, "On induction between parallel wires," *J. Soc. Telegraph Eng.*, vol. 9, no. 34, pp. 427–458, 1880, doi: 10.1049/jste-1.1880.0047.

[31] O. Heaviside, "On the electro-static capacity of suspended wires," *J. Soc. Telegraph Eng.*, vol. 9, no. 31, pp. 115–120, 1880.

[32] V. Alekseev, V. Petrov, and V. Naumov, "Invariance of modal transformations of electrical values in traveling wave fault locator," in *Proc. Int. Conf. Ind. Eng., Appl. Manuf. (ICIEAM)*, May 2020, pp. 1–5, doi: 10.1109/ICIEAM48468.2020.9111912.

[33] J. A. B. Faria and J. H. Briceno, "On the modal analysis of asymmetrical three-phase transmission lines using standard transformation matrices," *IEEE Trans. Power Del.*, vol. 12, no. 4, pp. 1760–1765, Oct. 1997, doi: 10.1109/61.634202.

[34] A. D. Polyanin, *Handbook of Linear Partial Differential Equations for Engineers and Scientists*. Boca Raton, FL, USA: CRC Press, 2002.

[35] Y. Hase, *Handbook of Power System Engineering*. Wiley, 2007.

[36] S.-J. Huang and C.-T. Hsieh, "High-impedance fault detection utilizing a Morlet wavelet transform approach," *IEEE Trans. Power Del.*, vol. 14, no. 4, pp. 1401–1410, Oct. 1999.

[37] L. van der Sluis, *Transients in Power Systems*. Chichester, U.K.: Wiley, 2001.

[38] P. S. Addison, *The Illustrated Wavelet Transform Handbook*, 2nd ed. Evanston, IL, USA: Routledge, 2020. [Online]. Available: https://www.routledge.com/The-Illustrated-Wavelet-Transform-Handbook-Introductory-Theory-and-Applications/Addison/p/book/9780367574000

[39] A. Paolucci, *Lezioni Di Trasmissione Dell'Energia Elettrica*. Padova, Italy: CLEUP Editore, 1998.

[40] F. Lucas, P. Costa, R. Batalha, D. Leite, and I. Škrjanc, "Fault detection in smart grids with time-varying distributed generation using wavelet energy and evolving neural networks," *Evolving Syst.*, vol. 11, no. 2, pp. 165–180, Jun. 2020, doi: 10.1007/s12530-020-09328-3.
[41] M. Solanki, Y. H. Song, S. Potts, and A. Perks, "Transient protection of transmission line using wavelet transform," in *Proc. Developments Power Syst. Protection*, Jan. 2001, pp. 299–302, doi: 10.1049/cp:20010159.
[42] G. Biasiotti, S. D. Sessa, F. Sanniti, and S. Talomo, "Impact of the transformer stray capacitances on the ground mode current in unearthed OHL networks: Analysis of the travelling waves propagation," in *Proc. IEEE Int. Conf. Environ. Electr. Eng. IEEE Ind. Commercial Power Syst. Eur. (EEEIC/I&CPS Europe)*, Jun. 2023, pp. 1–6.

SEBASTIAN DAMBONE SESSA (Member, IEEE) was born in Venice, Italy, in 1981. He received the Dr.-Ing. degree in electrical engineering from the University of Padova, in 2010, and the Ph.D. degree in power systems analysis, in 2017. In 2022, he was appointed as an Assistant Professor with the Department of Industrial Engineering, University of Padova. His research interests include transmission line modeling, fault location algorithms, stationary electrochemical and hybrid energy storage, high voltage direct current installations, and power system management. He has been a member of Cigré working groups B1.47, B1.45, and B1.56. He is a member of Italian AEIT.

FRANCESCO SANNITI (Member, IEEE) was born in Feltre, Italy, in 1994. He received the Dr.-Ing. and Ph.D. degrees in electrical engineering from the University of Padova, Italy, in 2019 and 2023, respectively. He is currently a Research Fellow with the LTEE Laboratory, University of Padova. He is the coauthor of 23 scientific articles. His research interests include dynamic stability and control of power system restoration processes and of low-inertia systems. Other recent activities regard the implementation of new algorithms for the fault distance detection in single-ended traveling wave devices and the implementation of multi-period optimal power flow for transmission planning purposes. He is a member of Cigré and AEIT.

ALESSANDRO GRECO was born in Rome, Italy, in 1968. He received the master's degree in energy engineering from the University of Rome, in 2006. From 1988 to 2005, he was with Enel SpA, at the time Italian TSO and DSO. In particular, he dealt with grid calculations in static and dynamic regimes for the definition of special protection schemes for the national electricity system. Since 2005, he has been with Terna, the largest system operator in Europe. In particular, from 2005 to 2008, he was the Shift Head of the Grid Services and Production Plans Control Room, and from 2008 to 2019, he was the Shift Coordinator of the Business Unit that deals with short and very short term planning of national production and energy exchanges with foreign countries, as well as procurement of services through the Ancillary Service Market. From 2019 to 2022, he was responsible for the adequacy and security of Italian electricity system, and since 2022, he has been responsible for the operational resilience of Italian HV transmission grids.

SIMONE TALOMO was born in Padua, Italy, in 1994. He received the master's degree in electrical engineering from the University of Padova, in 2019. Since 2019, he has been with Terna, the largest system operator in Europe. In particular, from 2019 to 2022, he dealt with the operational resilience of Italian HV transmission grids. Since 2022, he has been with the National Control Center, part of the dispatching and control–real time operation direction. His research interests include the definition of strategies, tools, and methods to support the real-time emergency management of high impact low frequency (HILF) events. This embraces the coordination with Regional Control Centers and other actors involved in the emergency, such as DSOs, Producers, and the Civil Protection Department.

MARTINA PAJUSSIN was born in Treviso, Italy, in 1992. She received the master's degree in electrical engineering from the University of Padova, in 2019. From 2019 to 2021, she was with Schneider Electric SE, a French multinational company specialized in digital automation and energy management. Since 2022, she has been with Terna, the largest system operator in Europe. She deals with the operational resilience of Italian HV transmission grids, specifically on fault location via traveling waves, tools for rapid recovery, and planning for the stock of compensating apparatus for the national power grids.

ROBERTO BENATO (Senior Member, IEEE) was born in Venice, Italy, in 1970. He received the Dr.-Ing. degree in electrical engineering from the University of Padova, in 1995, and the Ph.D. degree in power systems analysis, in 1999. In 2021, he was appointed as a Full Professor with the Department of Industrial Engineering, University of Padova. He is the author of 250 articles and seven books, edited by Springer, Wolters Kluwer, and China Machine Press. He has been a member of six Cigré working groups (WGs) and the Secretary of two joint WGs and the IEEE PES Substations Committee. In 2014, he was nominated as a member of IEC TC 120 "Electrical Energy Storage (EES) Systems" in the WG 4 "environmental issues of EES systems." He is currently a Corresponding Member of Cigré WG B1.72 "cable rating verification 2nd part." In 2018, he has been elevated to the grade of a CIGRÉ Distinguished Member. He is a member of Italian AEIT.

Open Access funding provided by 'Università degli Studi di Padova' within the CRUI CARE Agreement